

Cloud-Net+: A Cloud Segmentation CNN for Landsat 8 Remote Sensing Imagery Optimized with Filtered Jaccard Loss Function

Sorour Mohajerani, *Student Member, IEEE*, Parvaneh Saeedi, *Member, IEEE*

Abstract—Cloud Segmentation is one of the fundamental steps in optical remote sensing image analysis. Current methods for identification of cloud regions in aerial or satellite images are not accurate enough especially in the presence of snow and haze. This paper presents a deep learning-based framework to address the problem of cloud detection in Landsat 8 imagery. The proposed method benefits from a convolutional neural network (Cloud-Net+) with multiple blocks, which is trained with a novel loss function (Filtered Jaccard loss). The proposed loss function is more sensitive to the absence of cloud pixels in an image and penalizes/rewards the predicted mask more accurately. The combination of Cloud-Net+ and Filtered Jaccard loss function delivers superior results over four public cloud detection datasets. Our experiments on one of the most common public datasets in computer vision (Pascal VOC dataset) show that the proposed network/loss function could be used in other segmentation tasks for more accurate performance/evaluation.

Index Terms—Cloud detection, CNN, image segmentation, deep learning, Landsat 8, loss function, remote sensing, 38-Cloud.

I. INTRODUCTION

Cloud detection and cloud coverage estimation are two of the most critical steps in the analysis of remote sensing imagery. On one hand, transferring remotely sensed data from air/space-borne sensors to ground stations is an expensive process from time, cost, storage, and computational resources points of view. On the other hand, no useful information about the Earth's surface could be extracted from images heavily covered by clouds. Since, on average, 67% of the Earth surface is covered by clouds at any time [1], it seems that a considerable amount of resources can be saved by transferring images only with no/minimum amount of cloud coverage.

Cloud coverage by itself could provide useful information about climate parameters and natural disasters such as hurricanes and volcanic eruptions [2], [3]. Besides, the scattering and absorption characteristics of clouds vary with their micro-physical properties. Hence, detecting the presence of clouds over a region is important for deriving atmospheric parameters of that region [4]. As a result, identification of clouds in images is an important pre-processing step for many applications. This task is more difficult when only a limited number of spectral bands are available or utilized. It is worth noting that many air/spaceborne systems such as ZY-3, HJ-1, and GF-2 are equipped only with visible and near-infrared bands [5]–[7].

In recent years, many cloud detection algorithms have been developed. These methods can be divided into three main

categories: threshold-based [8], [9], handcrafted [10]–[12], and deep learning-based methods [13], [14].

Function of mask (FMask) [8], [15], [16] and automated cloud-cover assessment (ACCA) [9] algorithms are among the most known threshold-based algorithms for cloud identification. In these methods, a decision tree is used to label each pixel as cloud or non-cloud. In each branch of the tree, the decision is made based on the result of a thresholding function that utilizes one or more spectral bands of data. Haze optimized transformation (HOT) is among the group of handcrafted methods, which isolates haze and thick clouds from other pixels using the relationship between spectral responses of the red and blue bands. Yuan et. al. [11], proposed another handcrafted approach, which incorporates an object-based support vector machine (SVM) classifier to separate clouds from non-cloud regions using local cloud patterns.

With the recent advances made in deep-learning algorithms for image segmentation, several methods have been developed for cloud detection using deep-learning. Xie et al. [14] trained a convolutional neural network (CNN) from multiple small patches. The network classifies each image patch into one of the three classes of thin cloud, thick cloud, and non-cloud. As the output, it creates a probability map for each class. A major problem in cloud detection using deep-learning is the lack of accurately annotated ground truths since accurate manual annotation of images is a time consuming and tedious task. In addition, the default cloud masks provided with remote sensing products are mostly obtained through automatic/semi-automatic thresholding-based approaches and, unfortunately, they may not be very accurate. Authors in [13] have removed wrongly labeled icy/snowy regions in the default cloud masks in their dataset using a simple snow detection algorithm. They have shown that the performance of a cloud detection convolutional neural network (CNN) is improved by training on corrected ground truths.

Deep learning-based methods seem to be superior to threshold/handcrafted methods as they have delivered better results. However, most of those methods still cannot provide robust and accurate cloud masks in the scenes where bright/cold non-cloud regions are present alongside clouds [17].

Here, inspired by the progress made in deep learning techniques, we propose a new method to identify cloud regions and separate them from non-cloud ones in Landsat 8 images. Our proposed system is a fully convolutional neural network (FCN), which detects cloud pixels in an end-to-end manner. This network, which is named Cloud-Net+, is optimized with a novel loss function called Filtered Jaccard loss. As a result

S. Mohajerani and P. Saeedi are with the School of Engineering Science, Simon Fraser University, BC, Canada (e-mail: smohajer@sfu.ca, psaeedi@sfu.ca).

of utilizing this loss function, Cloud-Net+ is trained more accurately. This makes a difference in the performance of the system especially in images with no cloud.

Unlike FMask and ACCA, the proposed approach is not blind to the existing global and local cloud features in the image. In addition, since only four spectral bands—red, green, blue, and near-infrared (RGBNir)—are required for the system training and prediction, this model can be easily utilized for detection of clouds in images obtained from most of the existing satellites as well as airborne systems. Another advantage is that, unlike multitemporal methods such as the algorithm introduced in [12], the proposed method does not require prior knowledge of the scene such as cloud-free images. In addition, it is simple, straight forward, and can be used for other types of image segmentation applications. To the best of our knowledge, this is the first paper evaluating cloud detection performance on four public Landsat 8 cloud detection datasets.

In summary, the contributions of this work are as follows:

- Proposing Cloud-Net+, a modification to a previously introduced CNN [18], which can segment cloud pixels in remote sensing imagery. The blocks of Cloud-Net+ consist of multiple convolution layers and skip connections, which enable the model to learn cloud attributes properly. Also, an aggregation branch has been developed to retrieve cloud masks better.
- Proposing a novel loss function, which not only penalizes a model for poor prediction of clouds in images but also it *fairly* rewards correct prediction of non-cloud regions. Our experiments show that Filtered Jaccard loss outperforms another commonly used loss function for image segmentation. In addition, when Cloud-Net+ is trained with this loss function, it outperforms state-of-the-art cloud detection methods over four public datasets.
- Extending our public 38-Cloud dataset [18] for cloud detection in Landsat 8 imagery to 95-Cloud dataset. This new dataset—which has been made public—has 57 more Landsat 8 scenes (along with their manually annotated ground truths) than 38-Cloud dataset. Such a new dataset will help other researchers to improve the generalization ability of their cloud detection algorithms by training their models with more accurately annotated data.

The remainder of this paper has been organized as follows: in Section II, a summary of related works in cloud detection field has been reviewed. In Section III, our purposed method has been explained in detail. In Section IV, experimental results and discussions have been presented. At last, a conclusion in Section V summarizes our work.

II. RELATED WORKS

One of the first successful automatic cloud detection methods is Fmask (first version) [8]. In this algorithm, using seven bands of enhanced thematic mapper (ETM) and enhanced thematic mapper plus (ETM+) sensors, each pixel of an image was classified into five classes of land, water, cloud, shadows, and snow. The next version of Fmask [15] utilized cirrus band to distinguish cirrus clouds along with low altitude clouds. In the last version of Fmask (Fmask 4.0) [16], auxiliary data such

as digital elevation map (DEM), DEM derivatives, and global surface water occurrence (GSWO) have been incorporated with the other previously used bands. Although showing good results specially on Sentinel-2 images, the addition of those inputs makes Fmask 4.0 more complicated and difficult to use.

Since clouds move over the Earth's surface, multitemporal methods have also been investigated for cloud detection. Mateo-García et al. in [12] have used cloud-free images of Landsat 8 scenes to identify potential clouds. Then, a clustering and some threshold-based post-processing steps helped the authors to generate final cloud masks. Zi et al. [19] have combined a threshold-based with a classical machine learning method. In their system, authors have been benefited from a superpixel segmentation in the first step. Then, they have classified these superpixels into three classes of "cloud", "potential cloud", and "non-cloud" using a Fmask-like decision tree. To identify the exact class of a "potential cloud" superpixel, a two-layer deep neural network was used. After that, a fully connected conditional random field (CRF) has been implemented to refine the boundaries of the cloudy regions in the final masks.

Many convolutional neural networks (CNN) have been developed for pixel-wise labeling tasks. Most of these networks have a fully convolutional architecture, inspired by U-Net [20]. U-Net is first introduced to segment specific regions in electron microscopic stack images. It is widely used in many computer vision applications [21]–[23]. It has also been utilized in [13] to identify clouds in Landsat 8 scenes. Mohajerani et al. [18] have trained a complex CNN with a new dataset. Their network, which is called Cloud-Net, segments clouds in an end-to-end manner without the need for complicated pre/post-processing steps. Yang et al. [24] proposed an FCN, which detects clouds in ZY-3 thumbnail satellite images. In their work, a built-in boundary refinement approach (BR blocks) has been incorporated into the proposed CDnet to avoid further post-processing. Mateo-García et al. [25] have tested a simplified U-Net for transfer learning of the cloud detection in Landsat 8 images to Proba-V satellite images. They have shown that in the case of lack of Proba-V ground truths for training, it is possible to train a system on Landsat 8 images (which their proper ground truths are more available) and then using the found weights to predict the cloud locations in Proba-V images. Recently, Jeppesen et al. [26] have been introduced RS-Net to identify clouds in Landsat 8 images. RS-Net is an FCN inspired by U-Net and it is trained with both automatically (Fmask) and manually generated ground truth images of two public datasets. The authors have shown that results obtained by weights trained with Fmask outperform the Fmask direct results. RS-Net, which is the state-of-the-art method, offers an accuracy of 92.10% over Biome 8 dataset. However, our proposed approach pushes this limit to 95.36%.

III. PROPOSED METHOD

In this section, the proposed methodology for addressing the problem of cloud detection is described. First, a brief explanation of the data provided by Landsat 8 is given. Next, the cloud detection model and details of the training are described. Then, the proposed loss function is explained.

TABLE I: Landsat 8 Spectral Bands.

Spectral Bands	Wavelength (um)	Res. (m)
Band 1 - Ultra Blue	0.435 - 0.451	30
Band 2 - Blue	0.452 - 0.512	30
Band 3 - Green	0.533 - 0.590	30
Band 4 - Red	0.636 - 0.673	30
Band 5 - Near-infrared (Nir)	0.851 - 0.879	30
Band 6 - Shortwave Infrared 1	1.566 - 1.651	30
Band 7 - Shortwave Infrared 2	2.107 - 2.294	30
Band 8 - Panchromatic	0.503 - 0.676	15
Band 9 - Cirrus	1.363 - 1.384	30
Band 10 - Thermal Infrared (TIRS) 1	10.60 - 11.19	100
Band 11 - Thermal Infrared (TIRS) 2	11.50 - 12.51	100

A. Landsat 8 Images

Landsat 8 is equipped with two optical sensors. One of these sensors is operational land imager (OLI) and the other one is thermal infrared sensor (TIRS). The specification of all Landsat 8's bands are shown in Table I. In this work, only four spectral bands—Band 2 to Band 5 (RGBNir)—are used.

B. Cloud Detection Model

An end-to-end segmentation of clouds in images requires a feed-forward encoder-decoder CNN, which is capable of capturing all fine and coarse cloud features and their neighboring pixels. Similar to other FCNs, the proposed network is made of two main arms: contracting arm and expanding arm. Multiple convolutional blocks in contracting and expanding arms derive the high-level semantic contexts from low-level features of the input image. In the training phase, the contracting arm extracts important cloud attributes. It also down-samples the input while increasing its depth. The expanding arm, on the other hand, utilizes those extracted features and builds a mask—with the same size as the input image. The network is fed with a multi-spectral input image and generates a grayscale cloud probability map of the input image.

Fig.1 illustrates the overview of the proposed network. We modified the architecture of the Cloud-Net in [18] to develop a more efficient model that is more sensitive to clouds. This network, which is called Cloud-Net+, consists of six contracting and five expanding blocks. Successive convolutional layers are the heart of the blocks in both arms. The kernel size and the order of these layers play crucial roles in the quality of activated features, and therefore, it affects the final cloud detection outcome directly. On one hand, it seems that as the number of convolutional layers increases in each block, the distinction of captured context by the model improves. On the other hand, utilizing more of those layers explodes the complexity of the model. To defeat this problem, we removed the middle 3×3 convolution layer in the last two contracting blocks and the first expanding block of Cloud-Net. This decreases the number of parameters of the network significantly since these layers are very deep and contain thousands of parameters. Then, in all of the contracting arm blocks, we added a 1×1 convolution layer between each two adjacent 3×3 convolution layers. Since the 1×1 convolution layer contains a small number of parameters, the total number of parameters of Cloud-Net+ is 10% less than that of Cloud-Net. Utilizing the 1×1 kernel size in convolutional layers is applied for the first time in [27] and its effectiveness is

shown in works such as [28]. We have noticed that employing such kernel in the expanding blocks does not yield to a better recovery of the low-resolution feature maps. Therefore, we did not add it to the expanding blocks. Instead, an aggregation branch has been added to combine all of the feature maps of the expanding blocks together. The aggregation branch itself consists of six up-sampling layers (with bilinear interpolation) following by a 1×1 convolution.

The rectified linear unit (ReLU) [29] is chosen as the non-linear activation function of all of the convolution layers. Maxpooling layers are used to reduce the spatial size of the feature maps and trainable convolution transposed layers are used to enlarge those in the contracting and expanding arms.

C. Training Details

The size of the input images of Cloud-Net+ is $192 \times 192 \times 4$. Four channels are stacked in the following order: red, green, blue, and Nir. A regular spectral band of Landsat 8 scenes is quite large—around 9000×9000 pixels. Training a fully convolutional network with such a large input size leads to hundreds of millions of parameters and plenty of convolutional layers. This is not practically possible. One way to overcome this problem is to keep the network relatively small while cropping the large input image into multiple smaller patches. As a result, each spectral band is cut into 384×384 non-overlapping pieces (utilizing overlapping patches increases the complexity of pre/post-processing steps as well as training time significantly without a significant effect on the quality of the generated output masks). These patches are resized to 192×192 and then are divided by 65535 to the range $[0, 1]$ before the training.

We randomly augmented the input patches using online geometric translations such as horizontal flipping, rotation by an angle randomly selected from $-20 : 2 : 20$, and scaling with a random scale from 1.2, 1.5, 1.8, 2, 2.2, 2.5. The activation function in the last convolution layer of the network is a sigmoid, which obtains the output cloud mask. Adam gradient descent [30] method is utilized for the optimizer.

The initial weights of the network are obtained by a Xavier uniform random initializer [31]. The initial learning rate for the training of the model is set to 10^{-4} . We applied the learning rate decay policy during the training. As a result, when the validation loss does not drop in more than 15 successive epochs, the learning rate is reduced by 70%. This policy is continued until the learning rate reaches to the value of 10^{-8} . The batch size is set to 6. The proposed network is developed using Keras deep learning framework [32] with a single GPU.

D. Loss Function

Soft Jaccard/Dice loss function has been widely used for optimization of many image segmentation models such as models in [33]–[37]. The formulation of soft Jaccard loss for two classes of "0" and "1" is as follows:

$$J_L(t, y) = 1 - \frac{\sum_{i=1}^N t_i y_i + \epsilon}{\sum_{i=1}^N t_i + \sum_{i=1}^N y_i - \sum_{i=1}^N t_i y_i + \epsilon}, \quad (1)$$

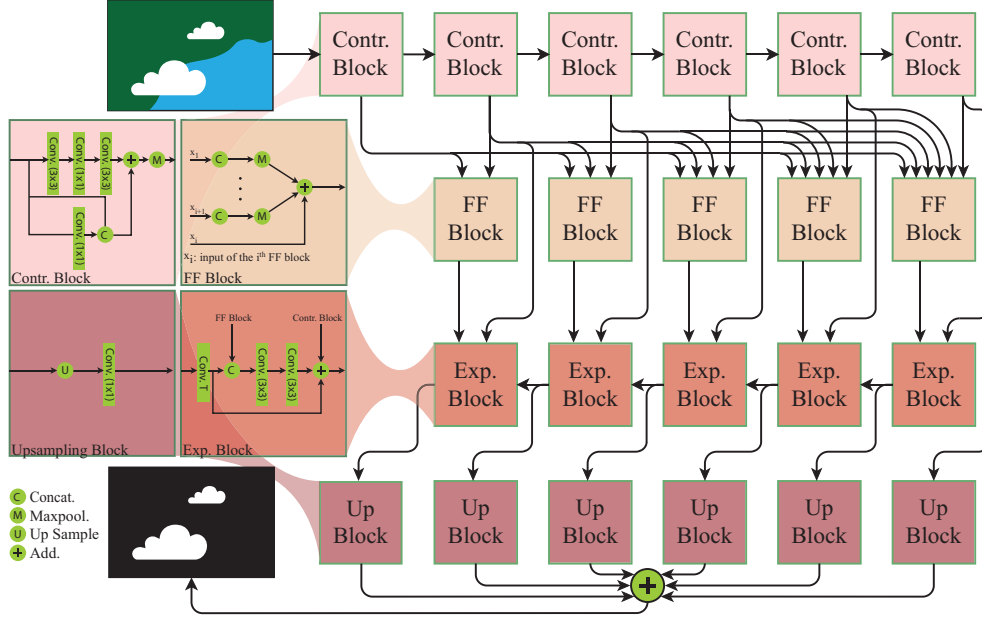


Fig. 1: Cloud-Net+ architecture in detail. In this figure, Concat., Add., and Maxpool. mean concatenation, addition, and maxpooling layers, respectively. FF, Exp., and Contr. represent the feedforward, expanding, and contracting blocks.

where t represents the ground truth and y is the output of the network. N denotes the total number of pixels in the t . $y_i \in [0, 1]$ and $t_i \in \{0, 1\}$ represent the i th pixel value of y and t , respectively and ϵ is set to 10^{-7} to avoid division by zero. However, this loss function has a defect in over-penalizing of cases with no class "1" in the ground truth.

Let's consider a small 2×2 input image with $t_0 = [0, 0; 0, 0]$ and two possible predictions of $y_1 = [0.01, 0.01; 0.01, 0.01]$ and $y_2 = [0.99, 0.99; 0.99, 0.99]$. It is clear that y_1 would be a better prediction than y_2 since it can be interpreted as having no class "1" in the input image. However, the soft Jaccard loss obtained by y_1 and y_2 are the same: $J_L(t_0, y_1) = J_L(t_0, y_2) \approx 1$. Consequently, network will penalize y_1 as much as it would penalize y_2 , even though y_1 represents a better prediction. Indeed, the major problem with this loss function is that whenever there is no class "1" in the ground truth, the numerator in Eq. (1) equals to ϵ (which is a really small number) and, as a result, the value of the loss approximates 1.

Observing this behavior, we propose a modified soft Jaccard loss function called Filtered Jaccard loss. The main idea behind the Filtered Jaccard function is to compensate for unfair values of the soft Jaccard loss and replace them with proper values whenever there is no class "1" in the ground truth. We can summarize the goal of Filtered Jaccard loss as follows:

$$Flt-J(t, y) = \begin{cases} G_L(t, y), & t_i = 0, \forall i \in \{1, 2, 3, \dots, N\} \\ J_L(t, y), & \text{Otherwise} \end{cases} \quad (2)$$

where $Flt-J$ denotes the Filtered Jaccard loss and G_L represents a compensatory function, which it will be defined later in this section. The condition in the first line of this equation indicates that when all of the ground truth pixels are equal to zero (no class "1" in ground truth), Filtered Jaccard loss uses G_L . Clearly, this condition can be rephrased as follows:

$$Flt-J(t, y) = \begin{cases} G_L(t, y), & (\sum_{i=1}^N t_i) = 0 \\ J_L(t, y), & (\sum_{i=1}^N t_i) > 0 \end{cases} \quad (3)$$

This formulation can be rewritten—in a more general form—as a combination of two functions of J_L and G_L , in which each of the functions are multiplied by ideal highpass and lowpass filters, respectively:

$$Flt-J(t, y) = k_G * G_L(t, y) * LP_{p_c}(\sum_{i=1}^N t_i) + k_J * J_L(t, y) * HP_{p'_c}(\sum_{i=1}^N t_i) \quad (4)$$

Here, LP_{p_c} denotes a lowpass filter with the cut-off point of p_c and $HP_{p'_c}$ denotes a highpass filter with the cut-off point of p'_c . k_G and k_J represent the coefficients for compensatory and Jaccard losses, respectively. The magnitude of both filters are limited in the $[0, 1]$ range. In Eq. (4), the value of LP_{p_c} is 0 when $(\sum_{i=1}^N t_i) > p_c$, so the value of $G_L(t, y) * LP_{p_c}$ becomes zero and, as a result, the Filtered Jaccard function in Eq. (4) will only have the soft Jaccard part. On the other hand, when $(\sum_{i=1}^N t_i) < p'_c$, $HP_{p'_c}$ becomes 0 and Filtered Jaccard function will be represented only by the G_L part. This behavior can be simply described as an automatic switch. To reach the exact goal depicted in Eq. (3), the cut-off point of the two ideal filters should be equal to each other, so they become complimentary of each other (only one becomes active at any time). Please note that, in signal processing literature, "cut-off" usually refers to the "frequency" at which the magnitude of a filter changes; however, in this work, cut-off is the "value" of $\sum_{i=1}^N t_i$ at which magnitude of the filter alters. Since this

transition should occur when $\sum_{i=1}^N t_i = 0$, the cut-off points are set to 0. This way, when no class "1" exists in the ground truth, G_L function is used for computing the loss value, and when

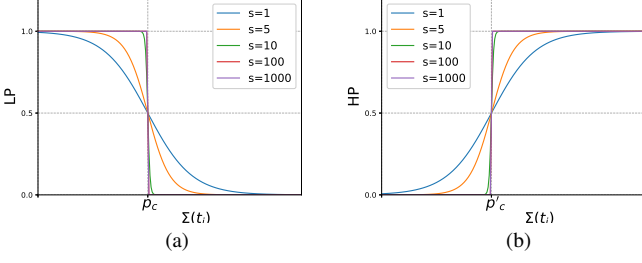


Fig. 2: Sigmoidal lowpass (a) and highpass (b) filters depicted in equations (5) and (6), respectively.

there exists class "1" in the ground truth, soft Jaccard function is utilized automatically. To have lowpass and highpass filters with nice gradient characteristics, inspiring by [38], we have used the sigmoid function as follows:

$$LP_{p_c}\left(\sum_{i=1}^N t_i\right) = \frac{1}{1 + \exp\left(s\left(\left(\sum_{i=1}^N t_i\right) - p_c\right)\right)}, \quad (5)$$

$$HP_{p'_c}\left(\sum_{i=1}^N t_i\right) = \frac{1}{1 + \exp\left(s\left(-\sum_{i=1}^N t_i + p'_c\right)\right)}. \quad (6)$$

where s denotes the steepness of the sigmoid transition. Fig. 2 illustrates these filters. By substituting equations (5) and (6) in Eq. (4), the Filtered Jaccard function will be described as:

$$\frac{k_G * G_L(t, y)}{1 + \exp\left(s\left(\left(\sum_{i=1}^N t_i\right) - p_c\right)\right)} + \frac{k_J * J_L(t, y)}{1 + \exp\left(s\left(-\sum_{i=1}^N t_i + p'_c\right)\right)} \quad (7)$$

If sigmoidal $LP_{p'_c}$ and $HP_{p'_c}$ as depicted in equations (5) and (6) were ideal filters, by setting $k_G = k_J = 1$ and $p_c = p'_c = 0$ in Eq. (7), the Filtered Jaccard loss would be identical to the one depicted in Eq. (3). But, unfortunately, they are not ideal filters. To keep the filters close to ideal, s is required to be a large number. We have set $s = 1000$ in our experiments to have fast transitions from 0 to 1 and vice versa in HP and LP , respectively. In addition, $p_c = p'_c$ are set to 0.5 (a number close to 0) to leave a safety margin and ensure that $LP_{0.5}\left(\left(\sum_{i=1}^N t_i\right) = 0\right) = 1$ and $HP_{0.5}\left(\left(\sum_{i=1}^N t_i\right) = 0\right) = 0$. k_G and k_J can be set to desired values to adjust the range of the loss during the training (shown in Fig. 2).

Naturally, the simplest candidate for the compensatory function is the following one, which we refer to it as "Inverted Jaccard" function:

$$G_L(t, y) \equiv InvJ_L(t, y) = 1 - \frac{\sum_{i=1}^N t'_i y'_i + \epsilon}{\sum_{i=1}^N t'_i + \sum_{i=1}^N y'_i - \sum_{i=1}^N t'_i y'_i + \epsilon}, \quad (8)$$

where $t' = 1 - t$ and $y' = 1 - y$ denote the complements of the t and y arrays, respectively. As it is clear from Eq. (8), Inverted Jaccard Loss is in fact the Soft Jaccard loss calculated by the complements of the ground truth and prediction arrays. Unlike Soft Jaccard loss, when there is no class "1" in the ground truth, the $\sum_{i=1}^N t'_i y'_i$ in the numerator of Eq. (8) is not equal to zero and, as a result, $InvJ_L(t, y)$ will lead to a fair value corresponding to a prediction. Having this function as the compensatory function in Eq. (7) delivers $Flt-J(t_0, y_1) =$

0.01 and $Flt-J(t_0, y_2) = 0.99$, which are the proper/expected loss values in our example. Please note that since Inverted Jaccard loss values are bound to range $[0, 1]$ and we have simply set $k_G = k_J = 1$, the overall error space will still be in range $[0, 1]$.

The most important advantage of Filtered Jaccard loss function is that the problem of over-penalizing in cases without class "1" is solved without adding any non-differentiable element or piecewise condition to the original soft Jaccard loss. Indeed Filtered Jaccard loss function smoothly switches between soft Jaccard and compensatory losses based on the existence of class "1" in the ground truth. In addition, since HP and LP filters are not functions of y , the gradient of Filtered Jaccard loss function is still nice (without any unwanted jump).

IV. EXPERIMENTAL RESULTS

In this section, a brief overview of the utilized datasets in this work is provided followed by evaluation metrics. Finally, the visual and numerical results over those datasets are reported and then discussed.

A. Datasets

1) *38-Cloud Dataset*: 38-Cloud dataset, which has been introduced in [18], consists of 38 Landsat 8 Collection 1 Level-1 scenes mainly selected from North America. 18 scenes belong to the training set and 20 scenes belong to the test set. The ground truths of these scenes are manually extracted. By cropping the scenes into $384 \times 384 \times 4$ non-overlapping pieces, the total number of patches reaches to 8400 for the training set and 9201 for the test set (each scene has been sufficiently zero-padded so that its size be divisible by 384).

All of the Landsat 8 scenes have triangle-like black (empty) margins around them. By eliminating training patches with more than 80% black pixels (less than 20% useful information), the number of informative patches reduces to 5155 training patches. This helps to reduce training time significantly.

2) *95-Cloud Dataset*: To improve the generalization ability of the deep neural networks trained on our 38-Cloud dataset, we have extended this dataset, which is called 95 cloud detection (95-Cloud) dataset (see Fig. 3). 57 new Landsat 8 scenes have been added to the 18 training scenes of 38-Cloud dataset. Therefore, in total, the new training set consists of 75 scenes. 38-Cloud test set has been kept intact in 95-Cloud dataset for evaluation consistency. The ground truths of these scenes are manually extracted. It is worth mentioning that different images in 95-Cloud are selected to cover many land cover types such as soil, vegetation, urban areas, snow, ice, water, haze, and different types of cloud patterns. The average cloud coverage percentage in the 95-Cloud dataset images has been kept around 50%. After cropping the images, the total number of patches for the training is 34701 and the test is 9201. Removing the empty patches from 95-Cloud training set reduces the number of patches to 21502 informative training patches. This dataset has been made publicly available to the community at <https://bit.ly/2kOoFMk>. The reader can also find detailed information about all of our experiments in this paper (such as the names of informative patches, training/test scene IDs, etc.) in the provided link.



Fig. 3: Locations of the 95-Cloud dataset scenes. Blue and orange points belong to training and test sets, respectively.

3) *SPARCS Dataset*: SPARCS dataset [39] consists of 80 patches of 1000×1000 extracted from Landsat 8 scenes gathered from around the world. The ground truths of the patches are manually generated. Each pixel is classified into one of the classes of "cloud", "shadow", "snow/ice", "water", "land", and "flooded". We have combined all the classes except "cloud" with each other under "clear" class to generate a binary mask for each patch. The total number of cropped patches in this dataset is 720.

4) *Biome 8 Dataset*: Biome 8 dataset is a publicly available dataset consisting of 96 Level 1 Landsat 8 scenes, which was first introduced in [40]. This dataset can be downloaded for free from [41]. The cloud ground truths of these images are manually generated for five classes of "cloud", "thin cloud", "clear", "cloud shadow", and "fill". We generated a binary ground truth out of Biome 8 ground truths by considering both "thin cloud" and "cloud" classes of this dataset as "cloud" and other three classes as "clear" class. The total number of cropped patches in this dataset is 44327.

B. Evaluation of the Model

After training of the proposed model with training patches of the above-mentioned datasets, the obtained weights are saved and used for the evaluation of the model by prediction over unseen test scenes of those datasets. First, the test patches, which are obtained by dividing a test scene into $384 \times 384 \times 4$ patches, are resized to $192 \times 192 \times 4$. Then, they are all fed to the model and the cloud probability map corresponding to each patch is retrieved. Next, those maps—which are grayscale images—are resized to 384×384 . These probability maps are then stitched up together to build up a cloud prediction map for each complete Landsat 8 scene. The mentioned procedure is repeated for all of the test scenes in a test set. To get a binary mask—out of a probability map—for a complete scene in a test set of a dataset, we use the very threshold which leads to the best cloud detection performance over the corresponding training set in that dataset.

C. Evaluation Metrics

When cloud masks of complete Landsat 8 scenes (including empty margins) are obtained by Cloud-Net+, they are compared against the corresponding ground truths. A predicted mask contains two classes of "cloud" (positive) and "clear" (negative). The performance of our algorithm is quantitatively measured by Jaccard index, precision, recall, specificity, and overall accuracy. These metrics are defined as follows:

$$\begin{aligned} \text{Jaccard Index} &= \frac{\sum_{i=1}^M tp_i}{\sum_{i=1}^M (tp_i + fp_i + fn_i)}, \text{Precision} = \frac{\sum_{i=1}^M tp_i}{\sum_{i=1}^M (tp_i + fp_i)}, \\ \text{Recall} &= \frac{\sum_{i=1}^M tp_i}{\sum_{i=1}^M (tp_i + fn_i)}, \text{Specificity} = \frac{\sum_{i=1}^M tn_i}{\sum_{i=1}^M (tn_i + fp_i)}, \\ \text{Overall Accuracy} &= \frac{\sum_{i=1}^M (tp_i + tn_i)}{\sum_{i=1}^M (tp_i + tn_i + fp_i + fn_i)}, \end{aligned} \quad (9)$$

where tp , tn , fp , and fn are the numbers of true positive, true negative, false positive, and false negative pixels in each test set scene. M denotes the total number of scenes in the test set. The Jaccard index is a widely accepted metric for measuring the performance of many image segmentation algorithms [36], [37]. This metric considers the regions in the predicted mask, which are correctly labeled as "cloud" and compares it to the union of the predicted mask and the ground truth.

D. Numerical and Visual Results

1) *Results over 38-Cloud Dataset*: Table II demonstrates experimental results of the proposed method trained on 38-Cloud training set and evaluated on its test set. There is also a comparison with other state-of-the-art methods on this dataset. We have evaluated the proposed Filtered Jaccard loss function with two different CNN architectures. One is Cloud-Net [18] and the other one is Cloud-Net+. Our experiments show that Filtered Jaccard loss outperforms soft Jaccard loss's results obtained by both architectures. For instance, when trained by Cloud-Net, Filtered Jaccard loss outperforms soft Jaccard by 1.4%. Cloud-Net+ also performs better when it is optimized using Filtered Jaccard loss—0.5% improvement compared to soft Jaccard.

The numerical results demonstrate that the proposed Cloud-Net+ captures more relevant features out of the input images and, therefore, generates cloud masks that are more similar to the manually extracted ground truths. As Table II indicates, the Jaccard index of Cloud-Net+ is better than that of Cloud-Net by 1.3%, when soft Jaccard loss is used in training. This amount of improvement is 0.4% for Filtered Jaccard loss. It is worth noting that Cloud-Net+ has 10% smaller number of trainable parameters than Cloud-Net and yet delivers superior performance. The combination of the proposed Cloud-Net+ with the proposed loss function delivers 4.5% and 3.4% higher Jaccard indices than the FCN in [13] and Fmask methods, respectively. The visual results of this dataset are shown in Fig.4.

2) *Results over SPARCS Dataset*: As suggested in [26], we have also randomly extracted 5 folds of images from SPARCS dataset. While conducting a 5-fold cross-validation over these folds, we got the first fold to test our proposed loss function. According to Table III, the Filtered Jaccard loss outperforms soft Jaccard (by 1.3% in Jaccard index with Cloud-Net and

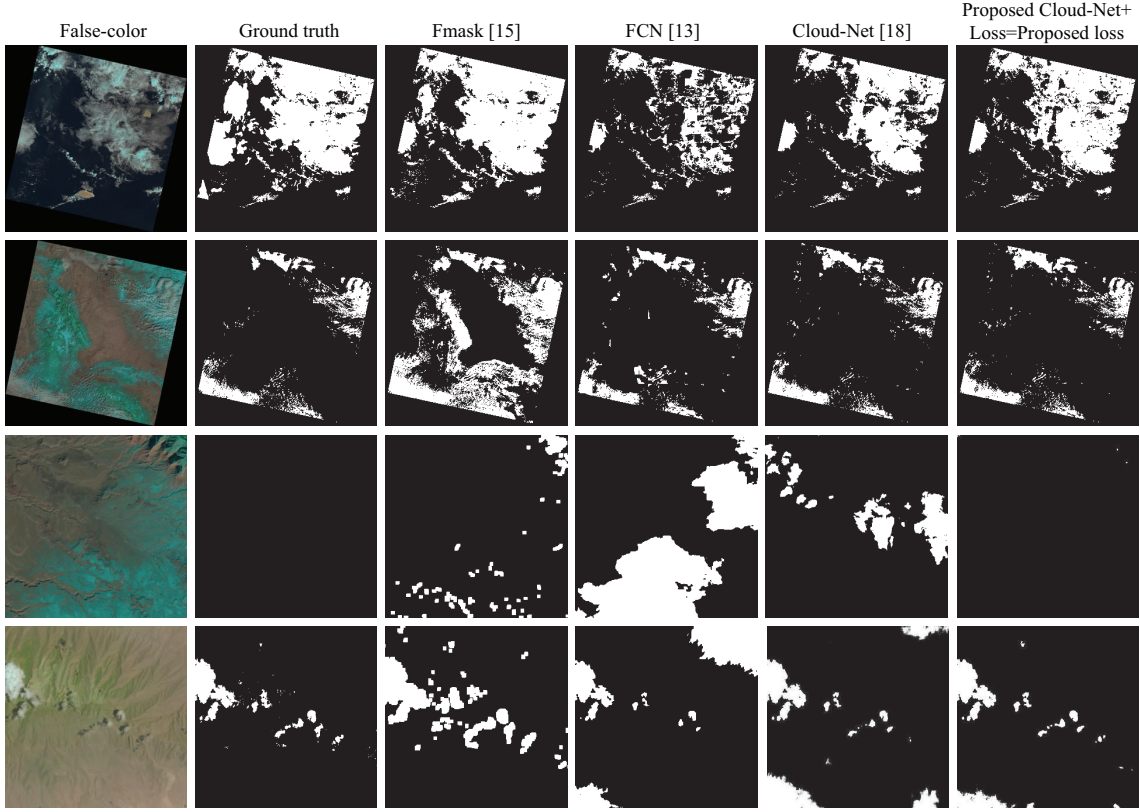


Fig. 4: Some visual examples of the results over 38-Cloud dataset.

TABLE II: Numerical performance over 38-Cloud dataset (in %).

Method	Training Patches	Loss	Jaccard	Precision	Recall	Specificity	Overall Accuracy
FCN [13]	All patches	J_L	85.03	96.15	88.02	98.34	95.05
Fmask [15]	NA	NA	85.91	88.65	96.52	94.20	94.94
Cloud-Net [18]	Informative patches	J_L	87.32	97.60	89.23	98.97	95.86
Cloud-Net	Informative patches	proposed $Flt-J$	88.55	97.63	90.49	98.97	96.26
Cloud-Net+	Informative patches	J_L	88.48	97.36	90.65	98.84	96.23
Cloud-Net+	Informative patches	proposed $Flt-J$	88.90	97.33	91.12	98.83	96.36

TABLE III: Numerical performance over SPARCS dataset (in %).

Method	Training set	Test set	Loss	Jaccard	Precision	Recall	Specificity	Overall Accuracy
Fmask [15]	NA	16 random images	NA	73.01	78.37	91.44	90.55	90.79
Cloud-Net [18]	64 random images	16 random images	J_L	81.64	92.15	87.73	97.20	94.62
Cloud-Net	64 random images	16 random images	proposed $Flt-J$	82.74	94.01	87.34	97.91	95.03
Cloud-Net+	64 random images	16 random images	J_L	83.34	92.38	89.48	97.24	95.12
Cloud-Net+	64 random images	16 random images	proposed $Flt-J$	84.66	92.90	90.51	97.41	95.53
RS-Net [26]	5-Folds Cross-Validation	5-Folds Cross-Validation	-	-	88.92	83.89	-	94.85
Cloud-Net+	5-Folds Cross-Validation	5-Folds Cross-Validation	proposed $Flt-J$	74.86	87.12	83.73	97.08	94.61

1.5% with Cloud-Net+). It also shows a better performance compared to Fmask (15.9% higher Jaccard index). Some visual results over this dataset with the comparison of different loss functions are shown in Fig. 5.

3) *Results over 95-Cloud Dataset:* Table IV demonstrates the experimental results of the proposed method on 20 test images of 95-Cloud dataset. Some visual examples of the predicted cloud masks are displayed in Fig. 6. Experiments show that the performance of Cloud-Net+ optimized with the proposed loss function is superior to that of Fmask algorithm. Cloud-Net+ delivers 6.5% greater Jaccard index compared to Fmask. In addition, as expected, the numerical results over the test set of this dataset are improved when they are

obtained by a network trained with more training images (95-Cloud training set is larger than 38-Cloud). To observe this difference, please note how the predicted cloud mask in the first row of Fig. 6 has been improved compared to the first row of Fig. 4.

4) *Results over Biome 8 Dataset:* To measure the performance of the proposed method on Biome 8 dataset, we have followed the instructions described in [26]. Therefore, we have randomly divided the dataset into two folds. For each biome, we have randomly selected two scenes for cloudy, two for midcloud, and two for clear categories. Therefore, we ended up with 48 scenes for fold 1 and 48 scenes for fold 2. Then, we conducted a 2-folds cross-validation experiment and

TABLE IV: Numerical performance over 95-Cloud dataset (in %).

Method	Training Patches	Loss	Jaccard	Precision	Recall	Specificity	Overall Accuracy
Fmask [15]	NA	NA	85.91	88.65	96.52	94.20	94.94
Cloud-Net [18]	Informative patches	J_L	90.83	97.67	92.84	98.96	97.00
Cloud-Net+	Informative patches	proposed $Flt-J$	91.53	97.13	94.06	98.69	97.22

TABLE V: Numerical performance over Biome 8 dataset (in %).

Method	Training set	Test set	Loss	Jaccard	Precision	Recall	Specificity	Overall Accuracy
Fmask [15]	NA	48 random scenes	NA	79.81	82.38	96.24	91.78	93.05
Cloud-Net [18]	48 random scenes	48 random scenes	J_L	84.84	93.92	89.78	97.72	95.48
Cloud-Net+	48 random scenes	48 random scenes	proposed $Flt-J$	85.45	93.77	90.59	97.59	95.60
RS-Net [26]	2-Folds Cross-Validation	2-Folds Cross-Validation	-	-	92.15	91.31	-	92.10
Cloud-Net+	2-Folds Cross-Validation	2-Folds Cross-Validation	proposed $Flt-J$	85.31	91.55	92.70	96.42	95.36
Multitemp. [12]	NA	2661 patches from 23 scenes	-	-	-	95.13	93.69	94.18
Cloud-Net+	64 random scenes	2661 patches from 23 scenes	proposed $Flt-J$	83.93	93.75	88.90	97.11	94.42
Simpl. U-net [25]	64 random scenes	32 random scenes	-	-	-	-	-	93.15
Cloud-Net+	64 random scenes	32 random scenes	proposed $Flt-J$	85.96	92.03	92.88	97.53	96.44

TABLE VI: Numerical performance for cross-dataset experiments (in %).

Method	Training set	Test set	Jaccard	Precision	Recall	Specificity	Overall Accuracy
Fmask [15]	NA	Entire Biome 8	74.76	78.16	94.50	89.19	90.73
Cloud-Net+	38-Cloud training set	Entire Biome 8	79.41	83.54	94.14	92.41	92.91
Cloud-Net+	95-Cloud training set	Entire Biome 8	82.66	87.06	94.24	94.26	94.26
RS-Net [26]	Entire SPARCS (all bands)	Entire Biome 8	-	86.96	95.45	-	90.96
RS-Net [26]	Entire SPARCS (all w/o thermal)	Entire Biome 8	-	88.72	94.49	-	91.59
RS-Net [26]	Entire SPARCS (RGBNir)	Entire Biome 8	-	89.04	88.49	-	89.25
Cloud-Net+	Entire SPARCS (RGBNir)	Entire Biome 8	75.74	86.97	85.43	94.76	92.05
Fmask [15]	NA	Entire SPARCS	62.00	65.25	92.57	88.15	89.01
Cloud-Net+	38-Cloud training set	Entire SPARCS	63.67	76.94	78.60	94.33	91.30
Cloud-Net+	95-Cloud training set	Entire SPARCS	61.26	74.14	77.90	93.47	90.45
Fmask [15]	NA	38-Cloud test set	85.91	88.65	96.52	94.20	94.94
Cloud-Net+	Entire SPARCS	38-Cloud test set	72.00	91.28	77.32	96.53	90.39
Cloud-Net+	38-Cloud training	38-Cloud test set	88.90	97.33	91.12	98.83	96.36
Cloud-Net+	95-Cloud training	38-Cloud test set	91.53	97.13	94.06	98.69	97.22

averaged the obtained numerical results of the two experiments to compare our results with the ones from RS-Net. The training has been done on informative patches of each fold with the proposed Filtered Jaccard loss. According to Table V, the proposed method offers 7% higher Jaccard index compared to Fmask. Additionally, Cloud-Net+ delivers better performance compared to RS-Net. The overall accuracy obtained by Cloud-Net+ is 3.5% higher than that of RS-Net. We have also compared the results of Cloud-Net+ with two other state-of-the-art methods (the Multitemporal model [12] and Simplified U-Net [25]). To have a fair comparison in both cases, we have used the same fraction of Biome 8 dataset. The specificity of Cloud-Net+ is 3.6% higher than that of Multitemporal model. Please note that this model requires a cloud-free image of a scene to generate the cloud masks of that scene and that is why it gives higher recall. Also, Cloud-Net+'s accuracy is 3.5% greater than that of Simplified U-Net. Some visual results over this dataset are shown in Fig. 7.

5) *Results of Cross-dataset Experiments:* To further measure the generalization ability of our method, we have done cross-dataset experiments—training on one dataset and testing on another dataset. The numerical results are reported in Table VI. According to this table, Cloud-Net+ (using Filtered Jaccard loss) outperforms RS-Net again for the training on SPARCS and test on Biome 8 dataset. Please note that

the overall accuracy obtained by Cloud-Net+ trained using RGBNir images is higher than that of RS-Net even when RS-Net has been trained by all 11 bands of Landsat 8. Another interesting point in this table is that since SPARCS is a relatively small dataset, training on it does not deliver the best results over larger datasets such as Biome 8 and 38-Cloud. On the contrary, training on 95-Cloud training set gives the best overall accuracy and Jaccard index on both Biome 8 and 38-Cloud datasets. This shows that having more training examples helps towards better generalization of methods.

6) *Experiment on Pascal VOC Dataset:* To test the proposed Filtered Jaccard loss function beyond the cloud detection datasets, we have conducted experiments over augmented Pascal VOC 2012 semantic segmentation dataset [42], [43]. This dataset contains 10582 images for training and 1449 for test. Each pixel in each image has been assigned to one of the existing 21 classes (including background class). Airplane, bicycle, cat, horse, and person are some of those classes. To obtain a binary segmentation, we have considered pixels belonging to only one of the classes—in particular, the person class, which is the most frequent one—as the positive class and every other pixel in all images (including background) are considered as the negative class.

We have utilized Cloud-Net+ for training (from scratch) and testing over Pascal VOC with the same setting as mentioned

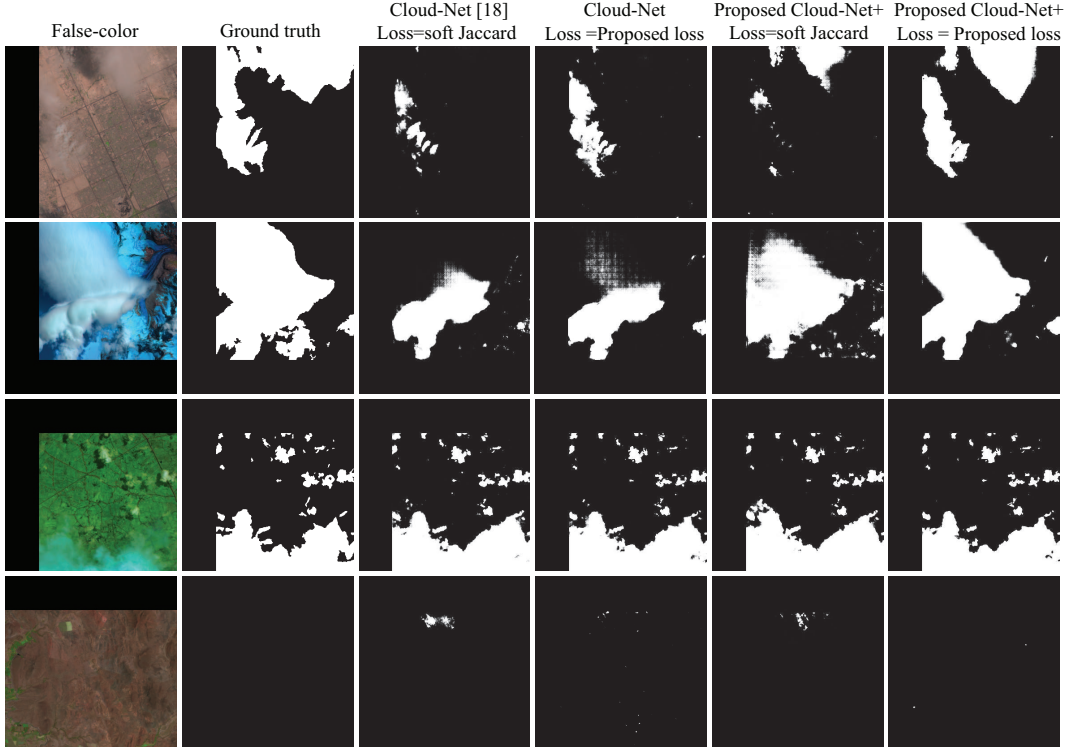


Fig. 5: Some visual examples of the results over SPARCS dataset obtained by different architectures and loss functions.

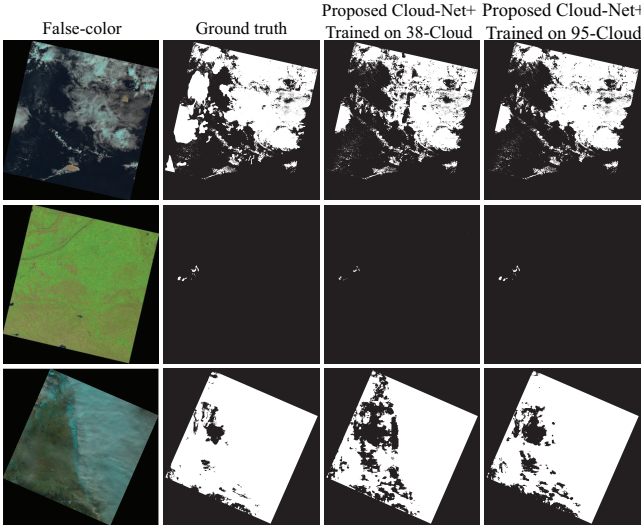


Fig. 6: Some visual examples of the results over 95-Cloud dataset.

in section III-B. The numerical results in Table VII indicates

TABLE VII: Numerical results over Pascal VOC dataset (in %).

Method	Loss	Jaccard	Overall Accuracy
Cloud-Net+	J_L	58.63	97.19
Cloud-Net+	$Flt-J$	63.11	97.59

that the proposed loss function outperforms soft Jaccard loss by 7.6% in Jaccard index. This shows that the proposed loss function works nicely with other type of images as well as remote sensing ones, which demonstrates the applicability of the proposed loss for different computer vision tasks. Two visual results are displayed in Fig. 8.

V. CONCLUSION

In this work, we have addressed the problem of cloud detection in Landsat 8 imagery using a deep learning-based

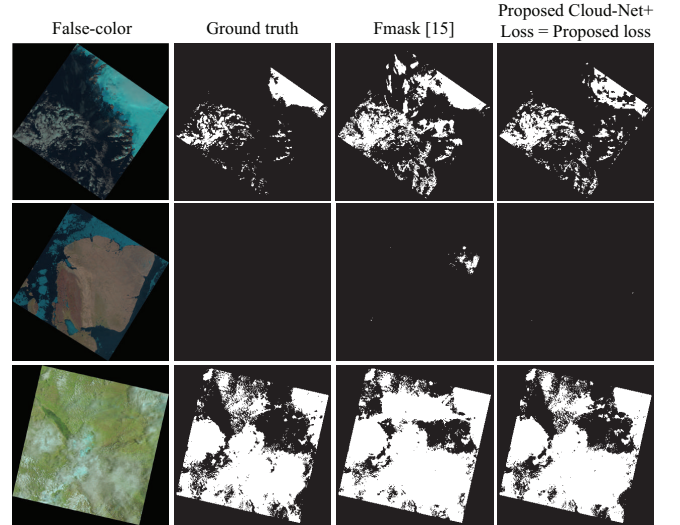


Fig. 7: Some visual examples of the results over Biome 8 dataset.

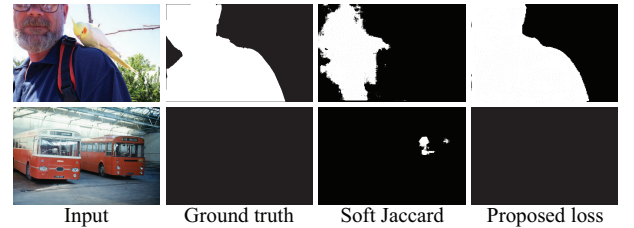


Fig. 8: Two examples of visual results on Pascal VOC dataset.

algorithm. The proposed network, Cloud-Net+, benefits from multiple convolution blocks to extract global and local features of clouds. This network which outperforms its parent, Cloud-Net, has been optimized using a new and novel loss function that reduces the number of misclassified pixels especially

when there are no cloud pixels in an image. The loss function can be used for other binary segmentation tasks, where the ground truth object exists only in some of the images. We have also released an extension to our previously introduced cloud detection dataset. It will help researchers to improve the generalization ability of their cloud segmentation algorithms.

REFERENCES

- [1] M. D. King, S. Platnick, W. P. Menzel, S. A. Ackerman, and P. A. Hubanks, "Spatial and Temporal Distribution of Clouds Observed by MODIS Onboard the Terra and Aqua Satellites," *IEEE Trans. on Geosc. and Rem. Sens.*, vol. 51, no. 7, pp. 3826–3852, 2013.
- [2] L. Zhu, M. Wang, J. Shao, C. Liu, C. Zhao, and Y. Zhao, "Remote Sensing of Global Volcanic Eruptions Using Fengyun Series Satellites," in *IEEE Int. Geosc. and Rem. Sens. Simp. (IGARSS)*, 2015, pp. 4797–4800.
- [3] R. S. Reddy, D. Lu, F. Tuluri, and M. Fadavi, "Simulation and Prediction of Hurricane Lili During Landfall over the Central Gulf States Using MMS Modeling System and Satellite Data," in *IEEE Int. Geosc. and Rem. Sens. Simp. (IGARSS)*, 2017, pp. 36–39.
- [4] C. R. Mirza, T. Koike, K. Yang, and T. Graf, "The Development of 1-D Ice Cloud Microphysics Data Assimilation System (IMDAS) for Cloud Parameter Retrievals by Integrating Satellite Data," in *IEEE Int. Geosc. and Rem. Sens. Simp. (IGARSS)*, vol. 2, 2008, pp. II–501–II–504.
- [5] Y. Jiang, G. Zhang, X. Tang, D. Li, W. Huang, and H. Pan, "Geometric Calibration and Accuracy Assessment of ZiYuan-3 Multispectral Images," *IEEE Trans. on Geosc. and Rem. Sens.*, vol. 52, no. 7, pp. 4161–4172, 2014.
- [6] Z. Wang, Z. Gao, Q. Li, W. Wang, L. Chen, and S. Li, "Urban aerosol monitoring over Ning-bo from HJ-1," in *IEEE Int. Geosc. and Rem. Sens. Simp. (IGARSS)*, 2012, pp. 2520–2523.
- [7] G. Gao and Y. Gu, "Tensorized Principal Component Alignment: A Unified Framework for Multimodal High-Resolution Images Classification," *IEEE Trans. on Geosc. and Rem. Sens.*, vol. 57, no. 1, pp. 46–61, 2019.
- [8] Z. Zhu and C. E. Woodcock, "Object-Based Cloud and Cloud Shadow Detection in Landsat Imagery," *Remote Sensing of Env.*, vol. 118, pp. 83–94, 2012.
- [9] R. R. Irish, J. L. Barker, S. Goward, and T. Arvidson, "Characterization of the Landsat-7 ETM+ Automated Cloud-Cover Assessment (ACCA) Algorithm," vol. 72, pp. 1179–1188, 2006.
- [10] Y. Zhang, B. Guindon, and J. Cihlar, "An Image Transform to Characterize and Compensate for Spatial Variations in Thin Cloud Contamination of Landsat Images," *Remote Sensing of Env.*, vol. 82, no. 2, pp. 173–187, 2002.
- [11] Y. Yuan and X. Hu, "Bag-of-Words and Object-Based Classification for Cloud Extraction From Satellite Imagery," *IEEE Journal of Selected Topics in Applied Earth Obs. and Rem. Sens.*, vol. 8, no. 8, pp. 4197–4205, 2015.
- [12] G. Mateo-García, L. Gómez-Chova, J. Amors-Lpez, J. Muñoz-Mar, and G. Camps-Valls, "Multitemporal Cloud Masking in the Google Earth Engine," *Remote Sensing*, vol. 10, no. 7, 2018.
- [13] S. Mohajerani, T. A. Krammer, and P. Saeedi, "A Cloud Detection Algorithm for Remote Sensing Images Using Fully Convolutional Neural Networks," in *IEEE Int. Workshop on Multim. Sig. Proc. (MMSP)*, 2018, pp. 1–5.
- [14] F. Xie, M. Shi, Z. Shi, J. Yin, and D. Zhao, "Multilevel Cloud Detection in Remote Sensing Images Based on Deep Learning," *IEEE Journal of Selected Topics in Applied Earth Obs. and Rem. Sens.*, vol. 10, no. 8, pp. 3631–3640, 2017.
- [15] Z. Zhu, S. Wang, and C. E. Woodcock, "Improvement and Expansion of the Fmask Algorithm: Cloud, Cloud Shadow, and Snow Detection for Landsats 47, 8, and Sentinel 2 Images," *Remote Sensing of Env.*, vol. 159, pp. 269–277, 2015.
- [16] S. Qiu, Z. Zhu, and B. He, "Fmask 4.0: Improved Cloud and Cloud Shadow Detection in Landsats 4–8 and Sentinel-2 Imagery," *Remote Sensing of Env.*, vol. 231, p. 111205, 2019.
- [17] S. Mohajerani, R. Asad, K. Abhishek, N. Sharma, A. v. Duynhoven, and P. Saeedi, "Cloudmaskgan: A Content-Aware Unpaired Image-To-Image Translation Algorithm for Remote Sensing Imagery," in *IEEE Int. Conf. on Image Proc. (ICIP)*, 2019, pp. 1965–1969.
- [18] S. Mohajerani and P. Saeedi, "Cloud-Net: An End-To-End Cloud Detection Algorithm for Landsat 8 Imagery," in *IEEE Int. Geosc. and Rem. Sens. Symp. (IGARSS)*, 2019, pp. 1029–1032.
- [19] Y. Zi, F. Xie, and Z. Jiang, "A Cloud Detection Method for Landsat 8 Images Based on PCANet," *Remote Sensing*, vol. 10, no. 6, 2018.
- [20] O. Ronneberger, P. Fischer, and T. Brox, "U-Net: Convolutional Networks for Biomedical Image Segmentation," *CoRR*, vol. abs/1505.04597, 2015.
- [21] Ö. Çiçek, A. Abdulkadir, S. S. Lienkamp, T. Brox, and O. Ronneberger, "3D U-Net: Learning Dense Volumetric Segmentation from Sparse Annotation," in *Medical Image Computing and Computer-Assisted Intervention (MICCAI)*. Springer Int. Publishing, 2016, pp. 424–432.
- [22] X. Yang, X. Li, Y. Ye, R. Y. K. Lau, X. Zhang, and X. Huang, "Road Detection and Centerline Extraction Via Deep Recurrent Convolutional Neural Network U-Net," *IEEE Trans. on Geosc. and Rem. Sens.*, pp. 1–12, 2019.
- [23] M. Yang, L. Jiao, F. Liu, B. Hou, and S. Yang, "Transferred Deep Learning-Based Change Detection in Remote Sensing Images," *IEEE Trans. on Geosc. and Rem. Sens.*, pp. 1–14, 2019.
- [24] J. Yang, J. Guo, H. Yue, Z. Liu, H. Hu, and K. Li, "CDnet: CNN-Based Cloud Detection for Remote Sensing Imagery," *IEEE Trans. on Geosc. and Rem. Sens.*, pp. 1–17, 2019.
- [25] G. Mateo-García and L. Gómez-Chova, "Convolutional Neural Networks for Cloud Screening: Transfer Learning from Landsat-8 to Proba-V," in *IEEE Int. Geosc. and Rem. Sens. Simp. (IGARSS)*, 2018, pp. 2103–2106.
- [26] J. H. Jeppesen, R. H. Jacobsen, F. Inceoglu, and T. S. Toftegaard, "A Cloud Detection Algorithm for Satellite Imagery Based on Deep Learning," *Remote Sensing of Env.*, vol. 229, pp. 247–259, 2019.
- [27] M. Lin, Q. Chen, and S. Yan, "Network In Network," *CoRR*, vol. abs/1312.4400, 2013.
- [28] S. Zagoruyko and N. Komodakis, "Wide Residual Networks," in *Proceedings of the British Machine Vision Conf. (BMVC)*, E. R. H. Richard C. Wilson and W. A. P. Smith, Eds., 2016, pp. 87.1–87.12.
- [29] V. Nair and G. E. Hinton, "Rectified Linear Units Improve Restricted Boltzmann Machines," in *Proceedings of Int. Conf. on Machine Learning (ICML)*, 2010, pp. 807–814.
- [30] D. P. Kingma and J. Ba, "Adam: A Method for Stochastic Optimization," *CoRR*, vol. abs/1412.6980, 2014.
- [31] X. Glorot and Y. Bengio, "Understanding the difficulty of training deep feedforward neural networks," in *Proceedings of Int. Conf. on Artificial Intelligence and Statistics*, ser. Proceedings of Machine Learning Research, vol. 9. PMLR, 2010, pp. 249–256.
- [32] F. Chollet et al., "Keras," <https://keras.io>, 2015.
- [33] W. Waegeman, K. Dembczyński, A. Jachnik, W. Cheng, and E. Hüllermeier, "On the Bayes-optimality of F-measure Maximizers," *Journal of Machine Learning Research*, vol. 15, no. 1, pp. 3333–3388, 2014.
- [34] A. A. Novikov, D. Lenis, D. Major, J. Hladvka, M. Wimmer, and K. Bhlér, "Fully Convolutional Architectures for Multiclass Segmentation in Chest Radiographs," *IEEE Trans. on Medical Imaging*, vol. 37, no. 8, pp. 1865–1876, 2018.
- [35] Y. Yuan, M. Chao, and Y. C. Lo, "Automatic Skin Lesion Segmentation Using Deep Fully Convolutional Networks With Jaccard Distance," *IEEE Trans. on Medical Imaging*, vol. 36, no. 9, pp. 1876–1886, 2017.
- [36] S. Mohajerani and P. Saeedi, "Shadow Detection in Single RGB Images Using a Context Preserver Convolutional Neural Network Trained by Multiple Adversarial Examples," *IEEE Trans. on Image Proc.*, vol. 28, no. 8, pp. 4117–4129, 2019.
- [37] S. Mohajerani and P. Saeedi, "CPNet: A Context Preserver Convolutional Neural Network for Detecting Shadows in Single RGB Images," in *IEEE Int. Workshop on Multim. Sig. Proc. (MMSP)*, 2018, pp. 1–5.
- [38] X. Lu, C. Ma, B. Ni, X. Yang, I. Reid, and M.-H. Yang, "Deep Regression Tracking with Shrinkage Loss," in *European Conf. on Computer Vision (ECCV)*, 2018.
- [39] M. J. Hughes and D. J. Hayes, "Automated Detection of Cloud and Cloud Shadow in Single-Date Landsat Imagery Using Neural Networks and Spatial Post-Processing," *Remote Sensing*, vol. 6, no. 6, pp. 4907–4926, 2014.
- [40] S. Foga, P. L. Scaramuzza, S. Guo, Z. Zhu, R. D. Dille, T. Beckmann, G. L. Schmidt, J. L. Dwyer, M. J. Hughes, and B. Laue, "Cloud Detection Algorithm Comparison and Validation for Operational Landsat Data Products," *Remote Sensing of Env.*, vol. 194, pp. 379–390, 2017.
- [41] U. S. G. Survey, *L8 Biome Cloud Validation Masks*. Geological Survey data release: USGS, 2016.
- [42] M. Everingham, L. Van Gool, C. K. I. Williams, J. Winn, and A. Zisserman, "The PASCAL Visual Object Classes Challenge 2012 (VOC2012) Results," <http://www.pascal-network.org/challenges/VOC/voc2012/workshop/index.html>.
- [43] B. Hariharan, P. Arbelaz, L. Bourdev, S. Maji, and J. Malik, "Semantic contours from inverse detectors," in *Int. Conf. on Computer Vision (ICCV)*, 2011, pp. 991–998.